LA-UR-18-20274 (Accepted Manuscript)

# Flow-through compression cell for small-angle and ultra-small-angle neutron scattering measurements

Hjelm, Rex Paul Jr.
Taylor, Mark
Frash, Luke
Hawley, Marilyn E.
Ding, Mei
Xu, Hongwu
Barker, John
Heath, Jason
Dewers, Thomas



**To be published in:** Review of Scientific Instruments

**DOI to publisher's version:** 10.1063/1.5022678

**Permalink to record:** http://permalink.lanl.gov/object/view?what=info:lanl-repo/lareport/LA-UR-18-20274

# Flow-Through Compression Cell for Small-angle and Ultra-small-angle Neutron Scattering Measurements.

*Rex P. Hjelm,[a]* Mark A. Taylor,[b] Luke Frash,[c] Marilyn E. Hawley,[d] Mei Ding,[c] Hongwu Xu,[c] John Barker,[e] Daniel Olds,[f] Jason Heath,[g] and Thomas Dewers[g]*

[a] *Materials Science in Radiation and Dynamics Extremes, Materials Science and Technology Division and the Los Alamos Neutron Science Center, Los Alamos National Laboratory, Los Alamos New Mexico, USA. Present address: National Security Education Center, Los Alamos National Laboratory and the New Mexico Consortium, Los Alamos New Mexico, USA.*

[b] *Engineering Services, Los Alamos National Laboratory (retired) , Los Alamos New Mexico, USA.*

[c] *Earth Systems Observations, Earth and Environmental Sciences Division, Los Alamos National Laboratory, Los Alamos New Mexico, USA.*

[d] *Engineered Materials, Materials Science and Technology Division, Los Alamos National Laboratory (retired, Los Alamos New Mexico, USA).*

[e] *National Center for Neutron Research, National Institute of Standards and Technology.*

[f] *the Los Alamos Neutron Science Center, Los Alamos National Laboratory, Los Alamos New Mexico, USA. Present address: Neutron Sciences Directorate, Oak Ridge National Laboratory, Oak Ridge, Tennessee, USA.*

[g] *Geomechanics, Sandia National Laboratories, Albuquerque, New Mexico, USA.*

** Corresponding author: hjelm@lanl.gov*



## ABSTRACT

*In situ* measurements of geological materials under compression and with hydrostatic fluid pressure are important in understanding their behavior under field conditions, which in turn provides critical information for applications-driven research. In particular, understanding the role of nano- to micro-scale porosity in subsurface liquid and gas flow is critical for high-fidelity characterization of transport and more efficient extraction of the associated energy resources. In other applications, where parts are produced by consolidation of powders by compression, the resulting porosity and crystallite orientation (texture) may affect its in-use characteristics. Small-angle neutron scattering (SANS) and ultra-small-angle neutron scattering (USANS) probe length scales relevant to this domain of porosity. Here we show the design, realization and performance of a novel neutron scattering sample environment, a specially designed compression cell, which provides compressive stress and hydrostatic pressures with effective stress up to 60 MPa, using the neutron beam to probe the effects of stress vector parallel to the neutron beam. We demonstrate that the neutron optics is suitable for the experimental objectives and that the system is highly stable to the stress and pressure conditions of the measurements.

## Introduction:

Understanding the effects of compressive stress and fluid pressure has important applications in gas and liquid transport and in elucidating mechanical deformation behavior of porous geological materials. While most considerations of the problems associated with geo-materials have been placed on scales of centimeters to kilometers, it has become increasingly evident that smaller length scales down through micrometer to nanometer are likely to be important determinants of the properties of these complex systems. There are a number of experimental techniques that have been traditionally used to characterize materials structures at these smaller length scales, such as transmission electron microscopy (TEM), scanning electron microscopy (SEM) and x-

ray tomography, which are common techniques for probing pores, void structure and connectivity, and element and mineral distributions in geo-materials. Each method has its limitations, particularly for *in situ* measurements emulating conditions that are present in reservoir porous media.

Neutron scattering techniques, specifically small-angle neutron scattering (SANS) and ultra-small-angle neutron scattering (USANS), provide an additional means of measuring pore structure in metamorphic rocks, [1-3] sandstone,[4, 5] shale, [6-12] coal [8] and clay [13, 14] from the nanometer through to the micrometer length scales. Because of the penetrability of neutrons, samples can be probed *in situ* under conditions emulating those prevalent in the field using robust pressurized sample environments. In addition, the difference in neutron scattering length from deuterium verses hydrogen is extremely useful in assessing pore and void connectivity by discriminating fluid accessible pores and voids from those that are inaccessible [10-12, 15-18] and provides a measurement of fluid accessible surface areas.[6-9, 15, 17] The general form of the method in SANS, contrast matching and contrast variation, has been demonstrated to have broad applications for studies of phase morphology in geosciences, [6, 7, 10] materials [15, 19-21] and biological sciences. [22, 23]

Here we describe the design, realization, and performance of a novel fluid flow through compression cell with optics suitable for use with SANS and USANS neutron beams. The device simultaneously applies uniaxial compressive (overburden) stress, $\sigma_{ax}$, and hydrostatic fluid (pore) pressure, $p$, with effective stress, $\sigma_e = \sigma_{ax} - p$, up to 60 MPa. In this design the incident neutron beam is parallel to the effective stress; thus, providing structural information perpendicular to the stress direction. In this geometry the sample may be mounted on various substrates, used as support and for distributing fluids to and from the entry and exit faces of the porous sample and allowing samples to be made as thin as needed to avoid multiple scattering. A control and data acquisition program, Disco, [24] provides programmable, automated control and data output of stress and pore pressure as a function of time. This sample environment is complementary to an earlier one, where the beam direction is perpendicular to the applied uniaxial stress, providing structural information along the stress direction.[13] The design of that pressure cell holds some similarities with the cell described here, as it is also a device allowing for flow through of fluids under hydrostatic pressure and compressions. However, that device is an oedometer; the sides of the sample are constrained, whereas those in the device described here are not. Furthermore, the geometry of the oedometer requires thicker samples along the beam direction, whereas there is greater latitude for sample thickness with the compression stress parallel to the beam direction, mitigating the complications from multiple scattering.[16, 25] Finally, because the robust mechanical design of the compressing ram requires a long channel for the incident beam (Figs.1 and 2), greater attention must be paid to the device acceptance angles and neutron optics than in the oedometer, which has significantly fewer optical constrains.

**Background:**

Gas and liquid transport in porous media and the effects of stress and fluid pressure on the fluid flow and media mechanical properties are important in several areas of primary concern in energy and environment and in other areas of practical geological interest, such as nuclear nonproliferation. The transport of gas and liquid in each of the relevant lithological formations requires detailed characterization of pore and pore connectivity and fluid accessibility under field conditions as inputs to the validation of transport models from pore scale (nm to μm) [26-28]

properties to larger length scales, such as the core scale (cm) upward to field scale (m to km) transport models.[29-32]

In a broader context pore structure is also important to materials science, where structure and connectivity of voids and pores are critical to understanding in-use properties of porous materials parts, such as metals, ceramics and other materials, produced by sintering.[15-17, 33-38]

Hydrocarbon recovery rates using the existing "*horizontal drilling and hydraulic fracturing*" (fracking) methods in shale oil/gas production, for example, are extremely low, less than 10% for oil and approximately 20% for gas.[39] Apparently this is related to the small porosity, from nm's to sub μm's and the low permeability ($10^{-16}$-$10^{-20}$ $m^2$) of tight shale formations.[40] The accessibility of water to shale nano pores and their interactions with water, the common media used in fracking operations, largely determine the permeability of intact shale matrix. Currently these aspects of shale are poorly understood, driving key scientific questions on the shale characteristics and how these affect behavior of the confined hydrocarbon fluids. SANS and USANS offer additional tools for measuring this accessible pore space over the nano- to micro-scales, providing better estimates of the amount of accessible reservoir oil and gas and enabling a fundamental understanding of permeability of tight rocks. Both aspects are needed to assess potential for multiphase flow and to optimize operational parameters for maximized hydrocarbon recovery.

The unique capability of USANS/SANS in characterizing pore structures has been recognized and used increasingly in the last 5 years as the only efficient technique widely applicable in characterizing shale reservoirs.[6-9] The present work and our other work on a similar device probing structure perpendicular to the neutron beam [13] extends current USANS/SANS experimental access to pore characterization under compressive stress and fluid hydrostatic pressure extending current capabilities for pore characterization under static conditions.

In clay-bearing rocks, such as shale, small pore sizes and high specific surface areas result in low permeability and high capacities for aqueous contaminants that contribute to desirable sealing behaviors in geologic waste storage.[41] Much of the porosity in clay rocks and engineered clay barriers is less than 10 nm in size.[18, 42, 43]

In the arena of national security and nuclear non-proliferation, detection, location, and identification of suspected nuclear explosions are United States security priorities. Pore scale properties, the geometric variation and the mechanical responses to explosion shock waves, are important in assessing and modeling underground nuclear explosion (UNE) events and how this affects the time-dependent environmental release of the products that are the direct physical signatures of UNEs. The prompt and delayed UNE product release depends on two interrelated aspects: the micromechanics of lithological formations and how pore scale structure affects larger scale fractures [27] and prompt and delayed transport properties of UNE radiological products [44] at the pore through the induced fracture scale [26-28, 45-47] to the field level.[48]

Because of the limitations of traditional techniques, most current knowledge of fluid behavior in shale nanopores has been obtained from computer simulations [49, 50] with few experimental data available. SANS/USANS data can thus provide a required validation of these modeling efforts

and will serve as input parameters for simulation of fluid flow behavior at reservoir stress, pressure, and temperature conditions.

In many materials, particularly those of interest in defense applications, consolidated parts are formed from powders into required shapes by high stress compression. The latent voids and crystallite orientation (texture) of the compressed materials impact the properties and performance of the consolidated part.[15, 36, 37] *In situ* studies of the material voids and texture changes during compression and the stress-strain behavior during the compression process will serve as input and validation for constitutive modeling [35] and performance characteristics [38] important in predicting age awareness and the influence of environmental factors on the safety and performance. These studies, thus, allow addressing current inadequacies in these essential predictive capabilities.

**Compression Cell Description**:

The assembled compression cell and its components are shown in cross section view in Figure 1 and an exploded assembly diagram in Figure 2. The sample is compressed along the incident neutron beam (Figs. 1 & 2) by a 2 inch (50.8 mm) diameter ram assembly fitted with a neutron window retainer. The retainer holds a 1 inch (25.4 mm) diameter, 0.394" (10 mm) thick neutron transparent window. The assembly compresses the sample against the static window retainer. Mechanical constrains requires that the incident neutron beam enters the sample chamber through a 0.45 inch (11.4 mm) diameter, 2.35 inch (59.7 mm) long channel in the ram assembly with a neutron window upstream from the sample chamber. A cadmium aperture no larger than ¼ inch (6.3 mm) diameter is placed at the incident beam entrance to meet the requirement that the SANS or USANS incident beam divergence is matched to the cell incident beam acceptance angle of 2.66°. The length of the incident beam channel required suppression of internal reflections using 0.125 nm thick Gd foil as a liner. The acceptable angle of the scattered beam is set by a 10° chamfer down stream from the scattered beam. Fluid pressure is applied through the fluid ports at the side of the sample chamber.

**Materials:**
The cell design required that it be operated at total stresses up to 69 MPa. Finite element analysis (FEA) of 4340 steel, annealed at 865°C, having a yield strength of 470 MPa, was found suitable for the fabrication of the cell body, ram and neutron window retainers to meet these specifications, with a safety factor greater than three, while minimizing neutron activation of these parts. Viton™ O-rings placed in the grooves along the edges of all internal parts and neutron windows (Figs. 1 and 2) were used to pressure seal all internal parts. We used 25.4 mm diameter and 10 mm thick cylindrical neutron windows, either sapphire with C-plane orientation or titanium-zirconium alloy, both materials, having yield strengths of 400 MPa, were found by FEA analysis to be suitable for use under the required specifications with a safety factor of six.

**Procedures**:
*Pressure system*:
A diagram of the pressure system, shown in Figure 3, uses two ISCO series 100DM syringe pumps for the application of the compressive stress (ISCO B) and hydrostatic fluid pressure (ISCO A). The inert gas cylinder allows for purging of the system before refilling with sample fluids and provides a pressure source for activation of the ISCO solenoid valves. The valve configurations allow for isolation of the inert gas cylinder, sample fill system, the pore pressure

from the ISCO B and the stress from ISCO A from each other during various stages of operation. The plumbing system incorporates burst disks with values below the maximum allowable working pressure (MAWP) of the pressure system components positioned to protect against failure of any isolated pressure source. The system is assembled on a moveable cart (Fig. 4) for ease of setup at the beam lines with ½" (13 mm) polycarbonate personnel barriers to provide protection from the pressurized system with easy access to all valves and ready visibility of pressure gauges. The compression cell was connected to the pressure system with flexible tubing to enable mounting of the pressure cell on beam lines NGB 30 M SANS or BT5 USANS at the National Center for Neutron Research (NCNR), National Institutes of Standards and Technology (NIST), Gaithersburg, Maryland. All tubing was rated to 103 MPa.

The compression cell and its pressure system was tested to 125% of its maximum design pressure (86 MPa) and held for at least 10 minutes in compliance with the Los Alamos National Laboratory (LANL) and NIST pressure safety requirements.

*Neutron Scattering Measurements*:
SANS measurements were done on NGB 30 m SANS at NCNR,[51] using an incident neutron wavelength, $\lambda$, of 5 Å, with $\Delta\lambda/\lambda = 0.14$ fwhm. The scattering angle, $2\theta$, allowed by the chamfer of the cell was limited to less than 10°; thus, the SANS instrument was configured for measurements of scattering intensity, $d\Sigma(Q)/d\Omega$, using sample to detector distances of 3 and 12 m, giving a useable measurement $Q$ range for the scattering intensity of 0.0023 to 0.167 $Å^{-1}$. The neutron wavelength was chosen to reduce multiple scattering prevalent in geomaterials. This and acceptance angle of the cell preclude the use of lenses to access the lower $Q$-values that otherwise would be available on tis SANS instrument.[52] Here, $Q = (4\pi/\lambda)\sin\theta$ is the scattering wave number. As the length scales probed in a scattering measurement go as $Q^{-1}$, these values correspond to length scales between approximately 43 and 0.6 nm.

USANS measurements were performed on the BT5 instrument at NCNR.[53] using the same samples as for SANS. BT5 USANS uses a pair of three bounce, channel cut, perfect silicon (2 2 0) crystals, one as a monochromator, the other as an analyzer. The incident neutron wavelength was 2.38 Å with a wavelength-spread $\Delta\lambda/\lambda$ of 0.059. The usable $Q$-range of the measurements was from $3\times10^{-5}$ to $3\times10^{-3}$ $Å^{-1}$, which corresponds to length scales from approximately 3.3 µm to 33 nm.

USANS data was corrected for slit smearing using the Lake algorithm incorporated in the NCNR data reduction software. [54, 55] However, as the desmearing algorithm requires azimuthally isotropic scattering,[54, 56] which is not the case in the particular samples we chose for this demonstration, the desmearing is corrected from the resulting distortion by rescaling $Q$ by the square root of the aspect ratio of the SANS data.[56]

The SANS and USANS data were placed on an absolute scale of differential scattering cross section per unit volume, $d\Sigma(Q)/d\Omega$ ($cm^{-1}$), using the direct beam method in the NCNR data reduction package [55], after subtraction of a similarly reduced background of the cell containing a quartz slide coated with the epoxy adhesive used to mount the samples.

For SANS measurements the cell was mounted on a Huber goniometer (Fig. 5) for positioning in the neutron beam. The cell is mounted with a ½ inch (12.6 mm) polycarbonate personnel protection barrier (Fig. 5). The sample was manually positioned on USANS BT-5. In both SANS

and USANS the empty cell was aligned with the aid of a laser coincident with the instrument optical axis. The alignment was then confirmed with a beam measurement with the empty cell.

*Samples*:
The samples used to demonstrate the pressure capabilities and optics of the cell were 300 µm thick shale specimens mounted on 24.5 mm diameter quartz discs. The samples were imbedded in fluid, typically a mixture of $D_2O/H_2O$ under vacuum for several hours until bubbles were no longer seen to emerge from the sample. The saturated samples were placed in the cell sample chamber for SANS and USANS measurements.

**Controls and Data Acquisition**:
The compression cell stress and pressure are controlled by an automated programmable IDL application called, "DIsco", available from Los Alamos National Laboratory.[24] The application's graphical user interface (GUI, Fig. 6) provides information on the states of the ISCO pumps and cell pressure and stress readouts. It also provides remote controls to operate the pressure system. The application reads comma delimited text scripts for automated control and data acquisition.

**Results**:
*Pressure and stress performance*:
Figure 7 shows a graph of data generated by DIsco for a typical pressure and stress protocol on the compression cell. Scripted automation controls the pumps to maintain a specified pressure, $p$ and axial stress, $\sigma_{ax}$, set points that were synchronized with the neutron scattering measurements. Each pump data readout is time stamped by the data acquisition system, allowing for coordination of the times to each of the neutron scattering measurements, R#, indicated by the thick black bars in Figure 7. The data show that the system was extremely stable once the set points were reached, with the exception of brief, transients in the applied axial stress, typically lasting a few but no more than 30 seconds. Once the set points were reached the root mean square standard deviations were typically 100 Pa for $\sigma_{ax}$ and 4 Pa for $p$.

*Optics*
The incident and scatter beam acceptance angles of the compressive cell, 0.45° and 10°, the former of which is dictated by the mechanics of the cell, must be matched to the available configurations for SANS and USANS. For SANS these conditions limits the closest sample to detector distance of 3 m and precluded the use of collimating lenses. The length of the cell required that the crystal analyzer of the BT5 USANS be moved farther away from its usual position from the sample.

Figure 8 illustrates the background measurement of the empty USANS camera in its normal configuration and a 5/8" (16 mm) beam aperture compared to the camera with the **compression cell** with no sample with the crystal analyzer moved down stream to accommodate the cell and a ¼ inch (6.3 mm) aperture. The detected primary beam intensity, which dominates the signal at low $Q$, was reduced by a factor of 0.16 with the cell and ¼ inch (6.3 mm) aperture compared to that measured with USANS in its normal configuration with 5/8 inch (16 mm). This value is completely consistent with the difference in aperture sizes; thus, moving the analyzer crystals down stream to accommodate the cell had no affect on measurement performance. More important is the comparison of the intensity over the higher $Q$ wings, where the data shows identical intensity, with only a small increase in the intermediate $Q$-domain in the presence of the cell as a result of a small amount of scatter from the sapphire windows. As instrument

background scatter dominates the higher $Q$ domain, this result demonstrates that the optics of the cell is well matched to that of the USANS, contributing very little to the instrument background. The USANS background measurement is a highly sensitive test of the cell optics.

A significant issue in the analysis of scattering data is possible multiple scattering. This effect distorts the scattering curve,[25] particularly with USANS,[33] significantly complicating the analysis.[25] In the absence of neutron absorption, the measured beam transmitted by the sample without scattering is a key indicator of the presence of multiple scattering. The transmission of the empty cell for USANS was greater than 0.995, consistent with the above observations, and 0.968 for SANS. These results give considerable latitude in meeting the total sample plus cell transmission of greater than 0.90 to assure negligible multiple scatter.

In principle an alloy of titanium (neutron scattering length, -3.44 fm) and zirconium (neutron scattering length, 7.16 fm) [57] will have zero average scattering length density with small residual fluctuations in Ti and Zr content over the length scale domains (greater than 1 nm) and thus very small to negligible SANS or USANS scattering for an alloy with volume faction 0.32 Ti. However, the Ti-Zr fabricated windows showed significant scattering in SANS and USANS measurements. Given the large difference in scattering length there will be significant scattering with even a small amount of phase separation of the components. This evidently this was the case with the material we used here.

The next step in the data reduction and the effects of the optics of the cell are shown in Figure 9, where the raw background data is plotted along with the raw sample data to show the Q-dependent signal to background from the cell. The values where the raw sample intensity falls below that of the background is a result of direct beam contamination of the scatter and the fact that the sample must transmit less of the direct beam than the background. As a result, data over these Q-values is not useful.

SANS data taken at the 12 m sample to detector position in Figure 10 of a shale sample mounted in the odometer for data taken under measurement R8 in Figure 5. The data, which is characteristic of all such samples mounted in the cell with an extremely clean background over higher scattering angles. As shale is a sedimentary rock it has a flattened structure parallel to the bedding plane, which shows anisotropic scatter for samples cut perpendicular to the bedding characteristic of these samples.[10, 56]

Combined reduced radial-averaged SANS and reduced and desmeared USANS data are shown in Figure 11. The USANS $Q$-values have been rescaled by $(b/a)^{1/2}$, where b/a is the aspect ratio of the long to short axes in the SANS intensity, given in Figure 10B.[56] This procedure corrects for the distortion from desmearing azimuthally anisotropic data and to bring the USANS data, which in this case sampled along the b axis of the scatter, onto the same bases as the radially averaged SANS data.[56] The final reduced data illustrates that the optics of the cell is sufficient to provide high quality low-$Q$ and ultra-low-$Q$ scattering data under elevated stress conditions to give useful data from the cell over the $Q$-domain from 3 $10^{-5}$ to slightly greater than 0.1 $Å^{-1}$.

**Conclusion:**

This new capability provides for *in situ* measurements needed to explore directly the responses of geo-material pore structure and the effects of pressurized fluids under field conditions. The

capability will provide new information to address issues in gas and oil production, latent nuclear product release and carbon sequestration among other high value applications.

**Acknowledgements**:
This work was funded by the Department of Energy (DOE), Office of Fossil Energy (FE), National Energy Technology Laboratory (NETL), under Grant Number FWP FE-406/408/409, entitled "Probing Hydrocarbon Fluid Behavior in Nanoporous Formations to Maximize Unconventional Oil/Gas Recovery". The design, fabrication and testing of the compression cell were carried out at the Los Alamos National Laboratory, which is operated by Los Alamos National Security, LLC, under DOE Contract DE-AC52-06NA25396. JH and TD were supported by the U.S. Department of Energy, Office of Science, Basic Energy Sciences under Award Number DE-SC0006883. Sandia National Laboratories is a multimission laboratory managed and operated by National Technology and Engineering Solutions of Sandia, LLC, a wholly owned subsidiary of Honeywell International, Inc., for the U.S. Department of Energy's National Nuclear Security Administration under contract DE-NA0003525. Access to the BT5 and NGB 30 m SANS instrument was provided by the Center for High Resolution Neutron Scattering, a partnership between the National Institute of Standards and Technology and the National Science Foundation under Agreement No. DMR-1508249. Certain commercial equipment is identified in the text to describe the instrument adequately. Such identification does not imply recommendation or endorsement by authors.

**References:**

1. L. M. Anovitz, D. R. Cole, D. D. Faulder, J. Sheets, H.-W. Wang, G. Rother, M. Wasbrough, R. Hjelm, M. Hartl, V. Pipich and Z. Fu, in *Proceedings, Thirty-eighth Workshop on Geothermal Reservoir Engineering* (Stanford University, Stanford, California, 2013), pp. 198-210.
2. L. M. Anovitz, G. W. Lynn, D. R. Cole, G. Rother, L. F. Allard, W. A. Hamilton, L. Porcar and M.-H. Kim, Geochimica et Cosmochimica Acta **73** (24), 7303-7324 (2009).
3. A. K. Navarre-Sitchler, D. R. Cole, G. Rother, L. Jin, H. L. Buss and S. L. Brantley, Geochimica et Cosmochimica Acta **109**, 400-413 (2013).
4. L. M. Anovitz, D. R. Cole, G. Rother, L. F. Allard, A. J. Jackson and K. C. Littrell, Geochimica et Cosmochimica Acta **102**, 280-305 (2013).
5. L. M. Anovitz, D. R. Cole, A. J. Jackson, G. Rother, K. Littrell, L. F. Allard, A. D. Pollington and D. J. Wesolowski, Geochimica et Cosmochimica Acta **158**, 199-222 (2015).
6. C. R. Clarkson, N. Solano, R. M. Bustin, A. M. M. Bustin, G. R. L. Chalmers, L. He, Y. B. Melnichenko, A. P. Radliński and T. P. Blach, Fuel **103**, 606-616 (2013).
7. X. Gu, D. R. Cole, G. Rother, D. F. R. Mildner and S. L. Brantley, Energy & Fuels **29** (3), 1295-1308 (2015).
8. M. Mastalerz, L. He, Y. B. Melnichenko and J. A. Rupp, Energy & Fuels **26** (8), 5109-5120 (2012).
9. L. F. Ruppert, R. Sakurovs, T. P. Blach, L. He, Y. B. Melnichenko, D. F. R. Mildner and L. Alcantar-Lopez, Energy & Fuels **27** (2), 772-779 (2013).
10. X. Gu, D. F. R. Mildner, D. R. Cole, G. Rother, R. Slingerland and S. L. Brantley, Energy & Fuels **30**, 4438-4449 (2016).

11. V. H. DiStefano, J. McFarlane, L. M. Anovitz, A. G. Stack, A. D. Gordon, K. C. Littrell, S. J. Chipera, R. D. Hunt, S. A. Lewis Sr., R. E. Hale and E. Perfect, Journal of Natural Gas Science and Engineering **35**, 646-660 (2016).
12. H. Xu, R. P. Hjelm, M. Ding, E. B. Watkins, Q. Kang and R. J. Pawar, in *Unconventional Resources Technology Conference (URTeC)* (2015).
13. T. A. Dewers, J. E. Heath, C. R. Bryan, J. T. Mang, R. P. Hjelm, M. Ding and M. A. Taylor, Environmental Science & Technology **52** (6), 3758-3768 (2018).
14. M. Ding, M. Hartl, H. Xu, R. P. Hjelm, A. Miller and Y. Wang, presented at the 2013 International High-Level Radioactive Waste Management, 2013 (unpublished).
15. J. T. Mang, Skidmore, C.B., Hjelm, R.P. and Howe, P.M., Journal of Materials Research **15**, 1199-1208 (2000).
16. J. T. Mang, R. P. Hjelm and E. G. Francois, Propellants, Explosives, Pyrotechnics **35**, 7-14 (2009).
17. J. T. Mang and R. P. Hjelm, Propellants, Explosives, Pyrotechnics **36**, 439-445 (2011).
18. L. M. Anovitz and D. R. Cole, in *Reviews in Mineralogy and Geochemistry*, edited by C. I. Steefel, S. Emmanuel and L. M. Anovitz (2015), Vol. 80, pp. 60-164.
19. Y. B. Melnichenko and G. D. Wignall, Journal of Applied Physics **102**, 021101 (2007).
20. R. P. Hjelm, American Chemical Society Symposium Series: Polymer Nanocomposites **804**, 71-84 (2002).
21. R. P. Hjelm, W. A. Wampler, P. A. Seeger and M. Gerspacher, Journal of Materials Research **9**, 3210-3222 (1994).
22. H. B. Stuhrmann, Journal of Physics: Conference Series **351**, 012002 (2012).
23. W. T. Heller, Acta Crystallographica Section D Biological Crystallography **66**, 1213-1217 (2010).
24. L. P. Frash, (Los Alamos National Laboratory, 2015).
25. S. Mazumder and A. Sequeira, Pramana—Journal of Physics **38** (2), 95-159 (1992).
26. T. W. Bowyer, C. Schlosser, K. H. Abel, M. Auer, J. C. Hayes, T. R. Heimbigner, J. I. McIntyre, M. E. Panisko, P. L. Peeder, H. Satorius, J. Schulze and W. Weiss, Journal of Environmental Radioactivity **59**, 139-151 (2002).
27. A. RØyne and B. Jamtveit, Reviews in Mineralogy and Geochemistry **80**, 25-42 (2015).
28. Y. Mehmani and M. T. Balhoff, Reviews in Mineralogy and Geochemistry **80**, 433-454 (2015).
29. D. J. DePaolo and F. M. Orr, Physics Today **61** (8), 46-51 (2008).
30. J. Samper, Z. Dai, J. Molinero, M. Garcia-Gutierrez, T. Missana and M. Mingarro, Physics and Chem. of the Earth **31**, 640-648 (2006).
31. A. Binley, S. S. Hubbard, J. Huisman, A. Revl, D. Robinson, K. Singha and L. Sater, Water Resource Research **51** (6), 3837-3866 (2015).
32. M. Ding, M. Geusebroek and H. A. Van der Sloot, in *Geochemical Engineering: Current Application and Future Trends*, edited by S. P. Vriend and J. J. P. Zijlstra (Elsevier Science B.V., 1998), pp. 319-324.
33. J. T. Mang and R. P. Hjelm, Propellants, Explosives, Pyrotechnics **38** (6), 831-840 (2013).
34. J. T. Mang, R. P. Hjelm, S. F. Son, P. D. Peterson and B. S. Jorgensen, Journal of Materials Research **22** (07), 1907-1920 (2007).

35. R. B. Schwarz, G. W. Brown, D. G. Thompson, B. W. Olinger, J. Furmanski and H. H. Cady, Propellants, Explosives and Pyrotechnics **38**, 685-694 (2013).
36. J. D. Yeager, D. J. Luscher, S. C. Vogel, B. Clausen and D. W. Brown, Propellants, Explosives and Pyrotechnics **41** (2016).
37. T. Willy, T. van Buuren, J. L. G. Overturf, K. J. Handly, B. Weeks and J. Ilavsky, Propellants, Explosives and Pyrotechnics **31**, 466–471 (2006).
38. R. Saurel, F. Fraysse, D. Furfaro and E. Lapebie, Computers & Fluids **159**, 95-111 (2017).
39. Z. Dong, S. A. Holditch and D. A. McVay, SPE Econ. Management **5**, 5-16 (2013).
40. M. E. Curtis, R. J. Ambrose, C. H. Sondergeld and C. S. Rai, edited by CUSG/SPE (2010).
41. I. Bibi, J. Icenhower, N. K. Niazi, M. Shahid and S. Bashir, in *Environmental Materials and Waste*, edited by M. N. V. Prasad and K. E. Shih (Academic Press, New York, 2016), pp. 543-567.
42. M. Holmboe, S. Wold and M. Jonsson, Journal of Contaminant Hydrololgy **128**, 19-32 (2011).
43. T. A. Dewers, J. Heath, R. Ewy and L. Duranti, International Journal of Oil, Gas and Coal Technology **5**, 229-248 (2012).
44. C. R. Carrigan, Y. Sun, S. L. Hunter, D. G. Ruddle, J. L. Wagoner, K. B. Myers, D. F. Emer, S. L. Drellack and V. D. Chipman, Scientific Reports **6**, 23032 (2016).
45. A. B. Jordan, P. H. Stauffer, E. E. Knight, E. Rougier and D. N. Anderson, Scientific Reports **5**, 18383 (2015).
46. C. R. Carrigan, R. A. Heinle, G. B. Hudson, J. J. Nitao and J. J. Zucca, Nature **382**, 528-531 (1996).
47. J. Schulze, M. Auer and R. Werzi, Applied Radiation and Isotopes **53**, 23-30 (2000).
48. Z. Dai, A. Wolfsberg, P. Reimus, H. Deng, E. Kwicklis, M. Ding, D. Ware and M. Ye, Journal of Hydrology **414-415**, 220-230 (2012).
49. H. Yoon and T. A. Dewers, Geophysical Research Letters **40**, 4294–4298 (2013).
50. T. W. Teklu, Alharthy, N., Kazemi, H., Yin, X., Graves, R. M., & AlSumaiti, A. M. , SPE Reservoir Evaluation & Engineering **17**, 168865 (2014).
51. C. J. Glinka, J. G. Barker, B. Hammouda, S. Krueger, J. J. Moyer and W. J. Orts, Journal of Applied Crystallography **31**, 430-445 (1998).
52. S.-M. Choi, J. G. Barker, C. J. Glinka, Y. T. Cheng and P. L. Gammel, Journal of Applied Crystallography **33**, 793-796 (2000).
53. J. G. Barker, C. J. Glinka, J. J. Moyer, M. H. Kim, A. R. Drews and M. Agamalian, Journal of Applied Crystallography **39**, 1004-1011 (2005).
54. J. A. Lake, Acta Crystallographica **23**, 191-194 (1967).
55. S. R. Kline, Journal of Applied Crystallography **39**, 895-800 (2006).
56. X. Gu and D. F. R. Mildner, Journal of Applied Crystallography **49**, 934-943 (2016).
57. V. F. Sears, Neutron News **3** (3), 26-37 (1992).

Figure Legends:

Figure 1: *Compression cell assembly in cross section.*
*The ram assembly, containing a sapphire neutron window, applies stress on the sample that is placed between the ram and a fixed plate, which holds a second neutron window. Hydrostatic fluid pressure is applied through the fluid ports. The incident neutron beam passes through a channel in the ram assembly, sapphire window and sample. The scattered beam exits the sample chamber through the second neutron window. A gadolinium foil lining controls reflections from the channel walls and the beam size is matched to the compression cell beam acceptance angles using a ¼ inch (6.3 mm) cadmium incident beam aperture.*

Figure 2: *Compression cell exploded assembly diagram.*

*Figure 3: Compression cell pressure system.*

*Figure 4: Compression cell pressure system in place on BT5, USANS.*

*Figure 5: Compression cell mounted on NGB 30 m SANS. Pore pressure fluid is injected from the left and overburden pressure fluid from the right. Neither line is connected to the pressure system in this picture.*

*Figure 6: DIsco GUI showing the graphical and digital data output, manual controls and programmable, script–generated controls.*

*Figure 7: Compression cell axial stress, fluid pressure and effective stress plotted from the output file of DIsco. Data: blue lines, pore or fluid pressure, p; black lines, axial stress, $\sigma_{ax}$;, red lines, effective stress, $\sigma_e$, = $\sigma_{ax}$ - p. The thick black bars indicate SANS measurement durations at each p and $\sigma_{ax}$ set point.*

*Figure 8: USANS background measurement. Data: ○, raw empty camera background in normal configuration using a 5/8" (16 mm) aperture; ●, raw background with empty compression cell and a ¼" (6.3 mm) aperture.*

*Figure 9: USANS raw and corrected sample data. Data: ○, raw background with an empty compression cell and a ¼ inch (6.3 mm) aperture, as in Fig. 8; □, raw shale sample data; ◆, empty cell background subtracted sample data after each has been corrected for transmission.*

*Figure 10: Data: A: raw SANS data taken at 12 m sample to detector distance of shale cut perpendicular to the bedding plane showing the expected asymmetry. Numbers on the left and bottom are detector pixel indices. Numbers on the right and top are Q-values. Here pore pressure = 12 MPa and effective stress = 8.1 MPa. B: trace of the SANS intensity over the annular ring, Q =0.02 Å$^{-1}$, shown in A, as a function of azimuth, Φ.*

Figure 11: Combined reduced SANS and desmeared USANS data of a shale sample in $D_2O$, for $p$ = 10 kPa and $\sigma_e$ = 45 MPa.

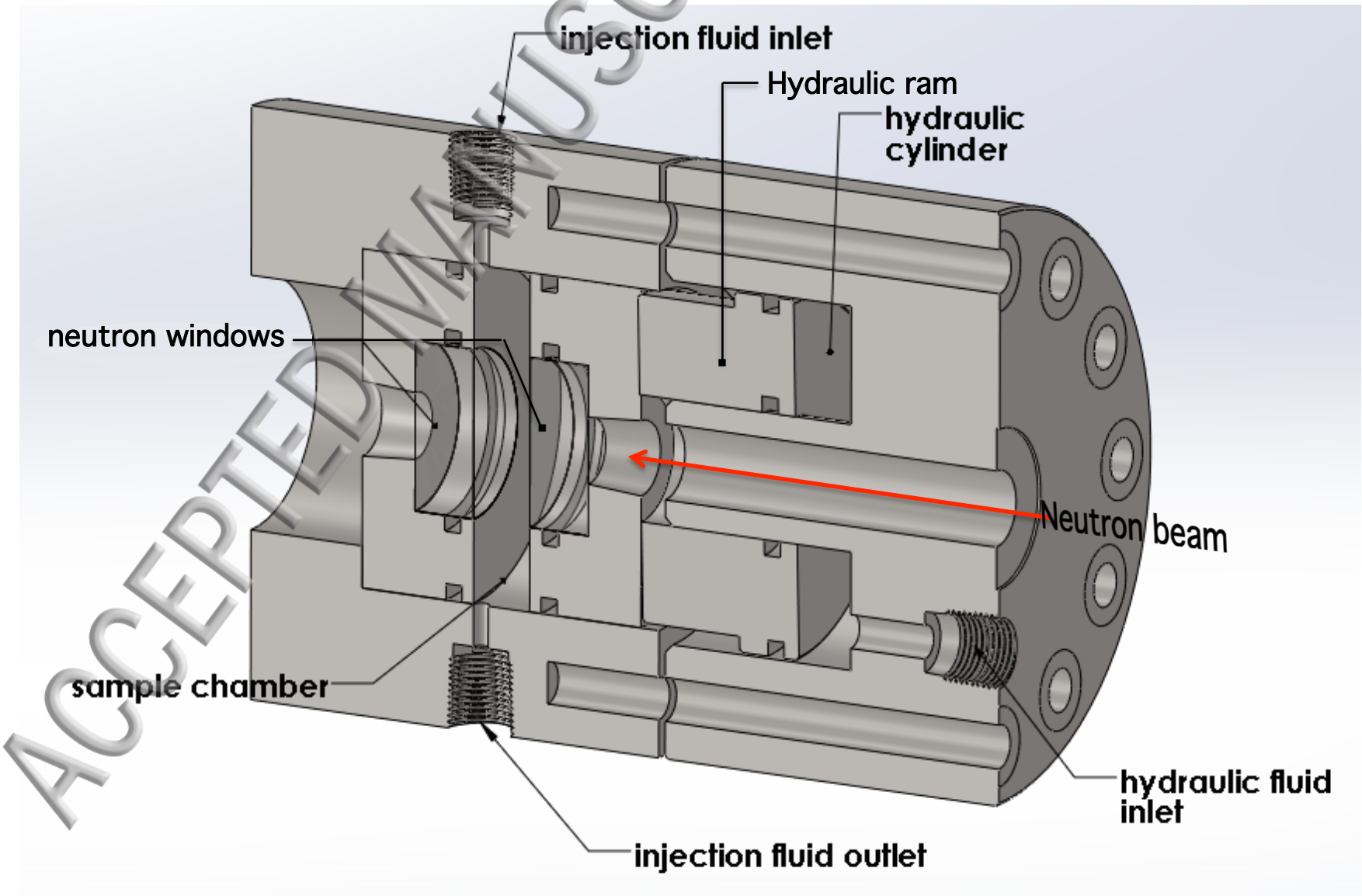

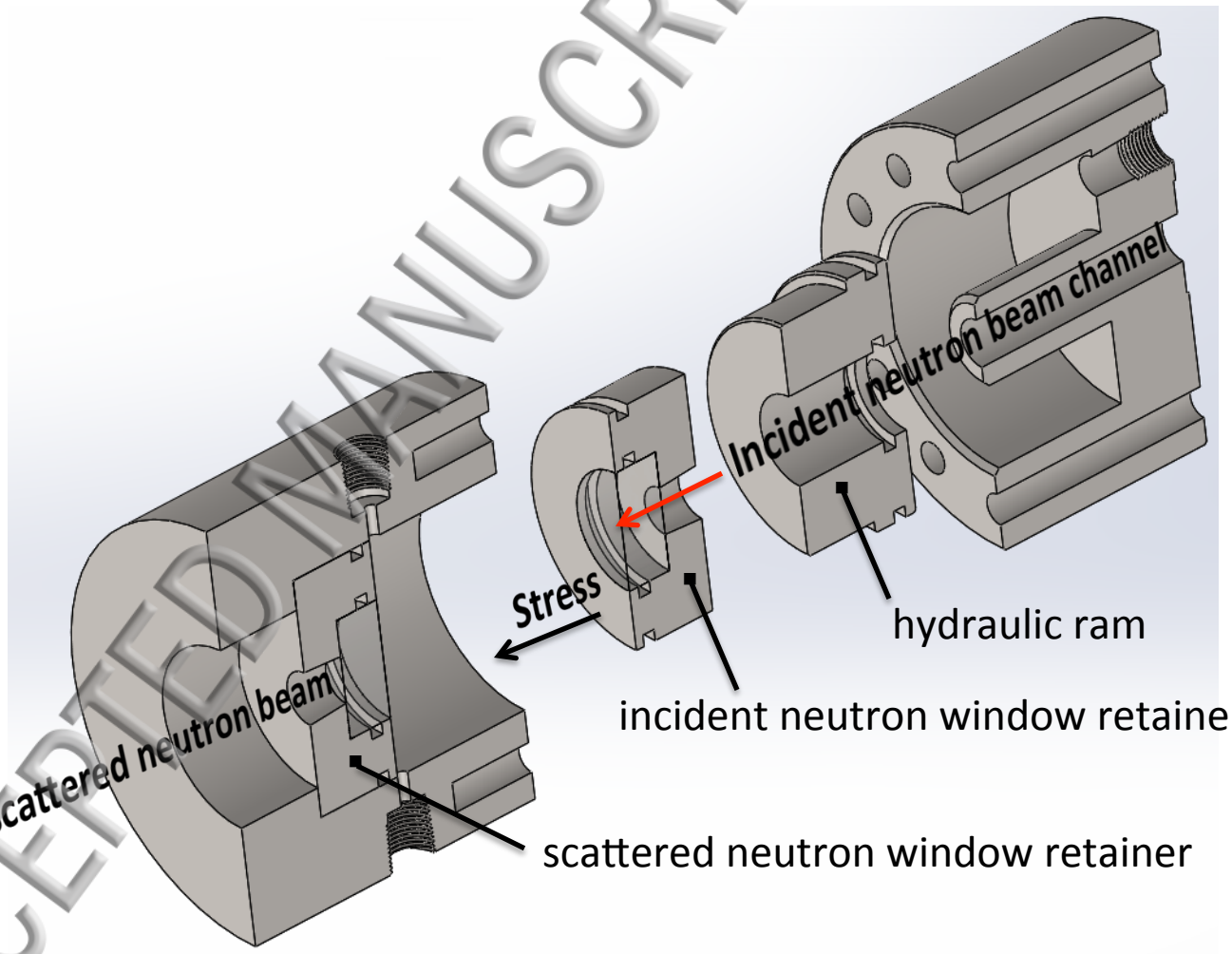

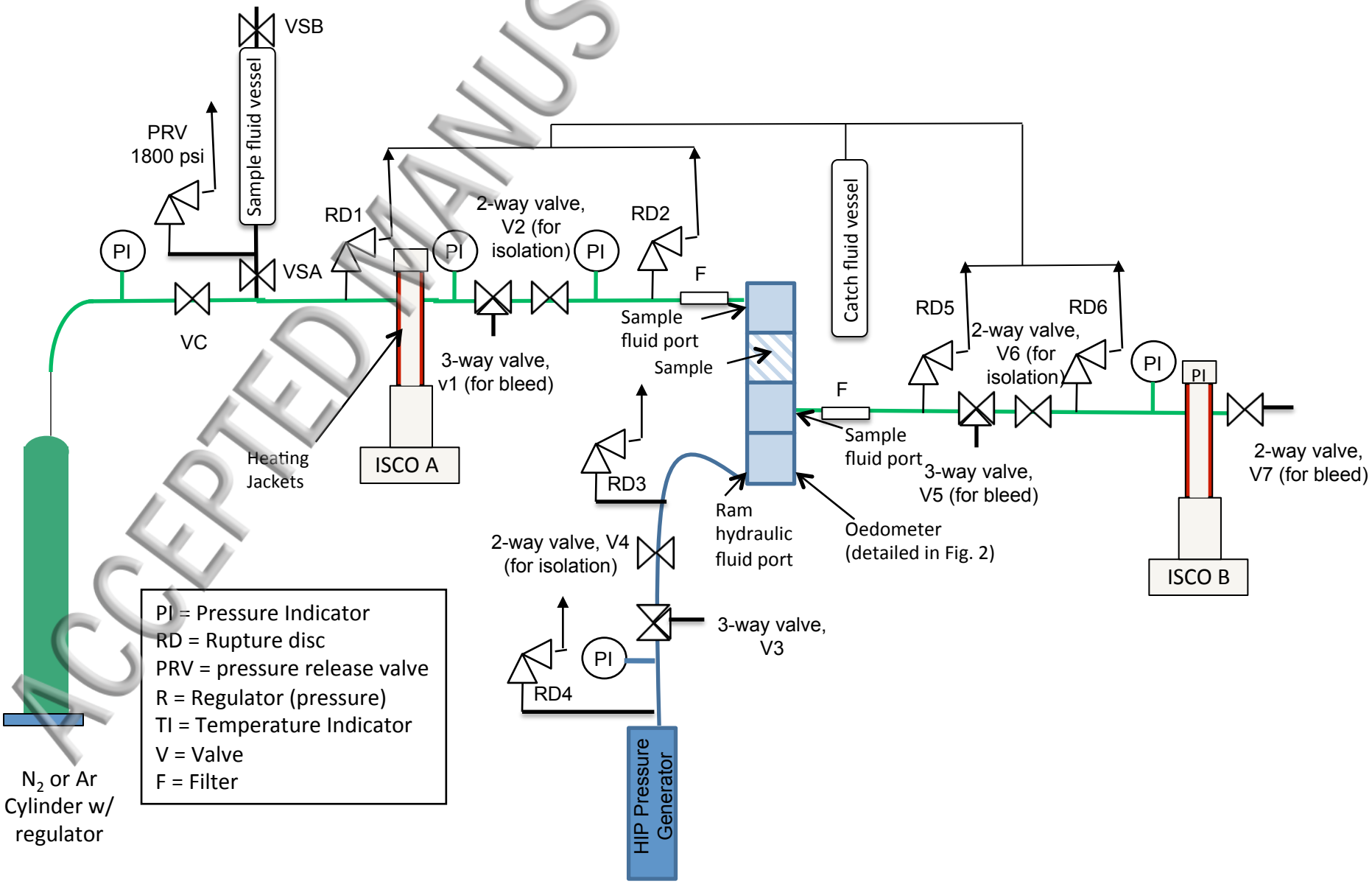

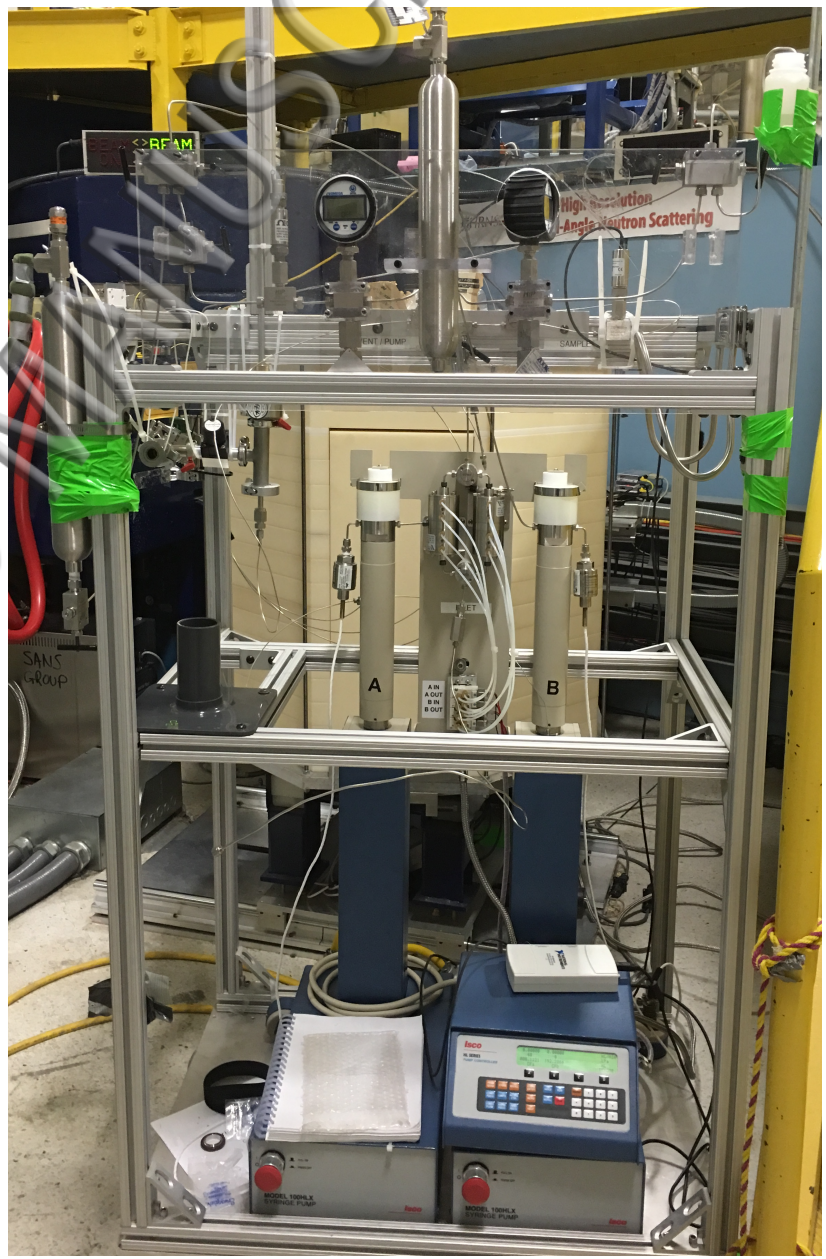

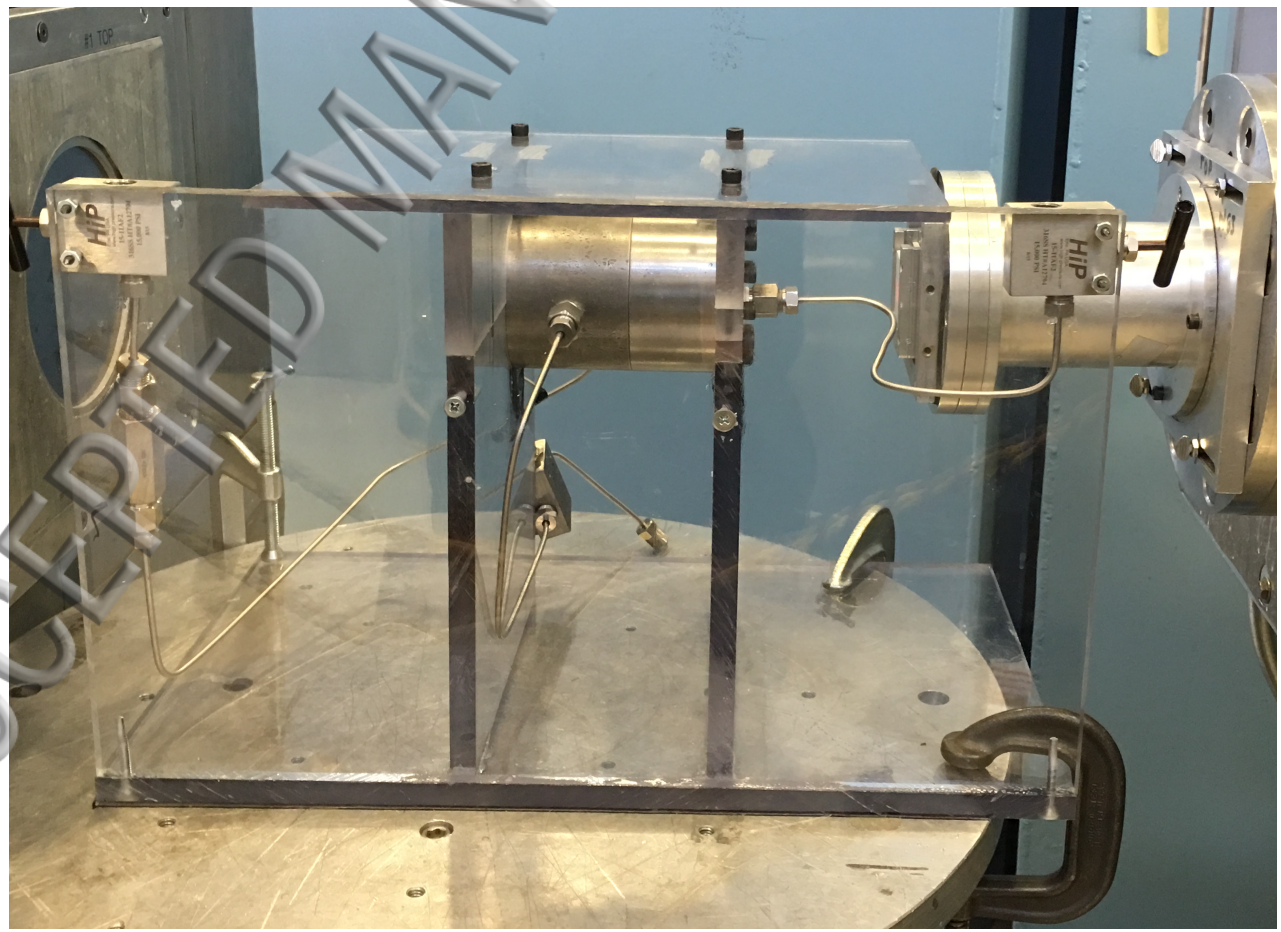

This manuscript was accepted by Rev. Sci.Instrum. Click here to see the version of record.

Output panel

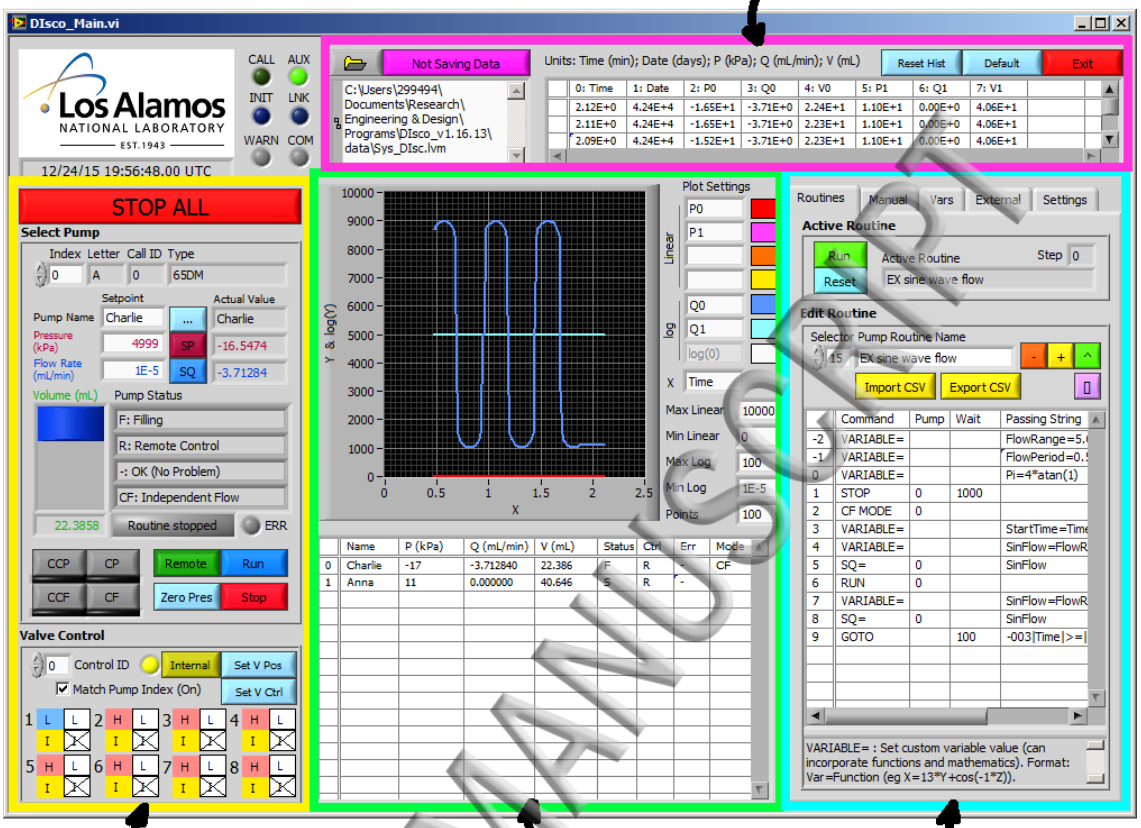


Pump control panel

Monitoring panel

Advanced control panel